Three-Dimensional Flow Patterns in Cracking Furnaces with Long-Flame Burners

Geraldine J. Heynderickx, Arno J. M. Oprins, and Guy B. Marin
Laboratorium voor Petrochemische Techniek, Krijgslaan 281(S5), B9000 Gent, Belgium

Erik Dick
Vakgroep Mechanica van Stroming, Warmte en Verbranding, St-Pietersnieuwstraat 41, B9000 Gent, Belgium

A 3-D computational fluid-dynamics model containing equations for mass, heat and momentum transfer and using a k-ϵ closure model, was used to calculate the 3-D flue-gas flow pattern and the corresponding 3-D temperature field for a pyrolysis furnace. The computational fluid dynamics model is combined with a reactor model for the cracking tubes and a radiation model for the radiative heat transfer in the furnace box. Detailed reaction kinetics for the naphtha cracking reactions in the tubes and a five-step reaction mechanism for the combustion of methane in the flames were used. This complete model reveals asymmetric flow patterns in a naphtha-cracking furnace with 4/2/1 split-coil reactors and fired with long-flame burners.

Introduction

Thermal cracking of hydrocarbons is an endothermal process that takes place in tubular reactor coils suspended in large gas-fired pyrolysis furnaces. Heat transfer to the reactor tubes is due to radiation from the furnace refractory walls, with temperatures up to 1,500 K, and to radiation from the flue gas with temperatures up to 2,100 K. Temperature profiles in the furnace, and therefore the type of burner that is used, influences radiation profiles to the reactor tubes. The furnaces are generally fired by radiation burners in the sidewalls of the furnace and/or by long-flame burners in the bottom of the furnace. The use of radiation burners in the sidewalls prevents the impact of flames on the reactor tubes, and reduces the presence of hot spots on the tube walls. These hot spots are detrimental for the lifetime of the tubes and result in higher coking rates, lowering the run length of the furnace between two decoking operations. The radiation burners are distributed over the total height of the furnace wall, thus assuring the injection of hot flue gas throughout the furnace. As a result, the heating of the reactor tubes throughout the furnace is more even. With long-flame burners, the height along which heat is generated in the furnace depends on the length of the flame. The flame length in turn is determined by, among other things, the degree of mixing from fuel gas and combustion air.

Correspondence concerning this article should be addressed to G. Heynderickx.

The heat-release profile in the furnace has a large influence on the heat fluxes to the reactor tubes determining the process gas temperature profiles and therefore the conversion of the process gas and the selectivity toward the different products.

The simulation of cracking furnaces with radiation burners is based on a furnace model using the zone method of Hottel and Sarofim (1967) for calculating the radiative heat transfer in the furnace (Plehiers and Froment, 1989), and on a reactor model with a detailed radical reaction scheme (Willems and Froment, 1988a,b; Ranzi et al., 1983; Dente and Ranzi, 1983). It is possible to predict the run length of such a furnace to within two to three days (Plehiers et al., 1990).

The simulation of long-flame fired furnaces with the same accuracy requires a model for the calculation of the flue-gas flow pattern (Sundaram and Albano, 1997) in the furnace and reaction kinetics for the combustion of the fuel gas in the flame. Determining accurate flow patterns in the furnace requires that the three-dimensional Navier-Stokes equations be solved (De Saegher et al., 1996; Detemmerman and Froment, 1998).

In the present article, a three-dimensional CFD model is used to calculate flow patterns and heat release in a naphtha-cracking furnace fired with long-flame burners. The calculation of the flow profiles is coupled to the calculation of the radiative heat exchange in the furnace and to calcula-

tion of the thermal cracking reactions in the reactor tube. Only a coupled simulation is capable of providing correct profiles.

Model Equations

Reactor model

A set of continuity equations for the different process gas species j is solved simultaneously with the energy and the pressure-drop equation.

$$\frac{dF_j}{dz} = \left(\sum_k n_{kj} r_{rk}\right)\frac{\pi d_t^2}{4} \tag{1}$$

$$\sum_j F_j c_{pj}\frac{dT}{dz} = Q(z)\pi d_t + \frac{\pi d_t^2}{4}\sum_k r_{rk}(-\Delta H)_k \tag{2}$$

$$\left(\frac{1}{M_m p_t} - \frac{p_t}{\alpha G^2 RT}\right)\frac{dp_t}{dz} = \frac{d}{dz}\left(\frac{1}{M_m}\right) + \frac{1}{M_m}\left(\frac{1}{T}\frac{dT}{dz} + fr\right), \tag{3}$$

with the friction factor (Knudsen and Katz, 1958),

$$fr = 0.092\frac{\mathrm{Re}^{-0.2}}{d_t} \tag{4}$$

for the straight parts of the reactor coils, and

$$fr = 0.092\frac{Re^{-0.2}}{d_t} + \frac{\chi}{\pi R_b} \tag{5}$$

for the tube bends, with (Nekrasov, 1969)

$$\chi = \left(0.7 + 0.35\frac{\Lambda}{90^\circ}\right)\left(0.051 + 0.19\frac{d_t}{R_b}\right). \tag{6}$$

A detailed radical reaction scheme for the thermal cracking of hydrocarbons, containing over 1,000 reactions between 128 species, is used to simulate the cracking reactions (Willems and Froment, 1988a,b).

The use of a one-dimensional plug-flow model in reactor tubes with smooth internal surfaces has a high degree of accuracy, since all radial profiles are wiped out due to the high turbulence corresponding to Reynolds numbers of 250,000.

Coke formation in the reactor tubes (Plehiers et al., 1990) is calculated from the corresponding continuity equation:

$$\frac{\partial C_C}{\partial t} = R_C. \tag{7}$$

Rate expressions for the coke formation in the thermal cracking of naphtha have been derived (Reyniers et al., 1994).

The calculation of the heat fluxes $Q(z)$ to the reactor tubes is based on the zone method of Hottel and Sarofim (1967). The furnace is divided into a number of surface and volume zones that are considered to be isothermal. For these zones the energy balances, containing radiative, convective, and conductive contributions, are constructed. The radiative contributions are obtained through Monte Carlo simulations, calculating the view factors between the different zones in the furnace. From these view factors, the total exchange areas Z_iZ_j between the zones are calculated. The total exchange area Z_iZ_j is the amount of radiative power emitted by zone Z_i in the direction of zone Z_j, divided by the black-body emissive power of the emitting zone. The black-body emissive power of zone i with temperature T_i is calculated from

$$E_i = \sigma T_i^4. \tag{8}$$

The set of energy balances for the furnace can be written as

$$\begin{pmatrix} Z_1Z_1 - \Sigma_j Z_1Z_j & Z_2Z_1 & \cdots & Z_nZ_1 \\ Z_1Z_2 & Z_2Z_2 - \Sigma_j Z_2Z_j & \cdots & Z_nZ_2 \\ \cdots & \cdots & \cdots & \cdots \\ Z_1Z_n & Z_2Z_n & \cdots & Z_nZ_n - \Sigma_j Z_nZ_j \end{pmatrix} \begin{pmatrix} E_1 \\ E_2 \\ \cdots \\ E_n \end{pmatrix} = \begin{pmatrix} Q_1A_1 \\ Q_2A_2 \\ \cdots \\ Q_nA_n \end{pmatrix}. \tag{9}$$

Furnace wall, process gas, and tube-skin temperature profiles in the furnace are obtained by solving the energy balances for the surface and volume zones of the furnace. Use of the accurate Hottel and Sarofim zone method results in an excellent prediction of the heat fluxes from the furnace to the reactor tubes.

Detailed information on coupled simulation of furnace and reactor is given by Rao et al. (1988) and Plehiers and Froment (1989).

Furnace

The model used to calculate the flue-gas flow pattern in the furnace is based on the Reynolds-averaged Navier-Stokes equations, containing a total continuity equation, a momentum equation, and an energy equation. Steady state is considered.

The total continuity equation is written as

$$\sum_{i=1}^{3}\frac{\partial}{\partial x_i}(\rho_g U_i) = 0. \tag{10}$$

The momentum equation in the i-direction,

$$\sum_{j=1}^{3}\frac{\partial}{\partial x_j}(\rho_g U_j U_i) = -\frac{\partial p}{\partial x_i} + \sum_{j=1}^{3}\frac{\partial}{\partial x_j}\left(\mu_t\left(\frac{\partial U_i}{\partial x_j} + \frac{\partial U_j}{\partial x_i}\right)\right) \tag{11}$$

states that the convective transport of the i-component of the momentum equals the sum of forces working in that direc-

tion, namely the pressure forces and the viscous forces due to velocity gradients. Other external force fields are negligible. For example, the impact of the gravitational force in the gas phase is limited due to the limited height differences in the furnace.

Because variations in temperature have an impact on gas densities, and thus on flow patterns, an energy equation is required:

$$\sum_{i=1}^{3}\frac{\partial}{\partial x_i}\left(\rho_g U_i(H+k+e_k)\right)-\sum_{i=1}^{3}\sum_{j=1}^{N}\frac{\partial}{\partial x_i}\left(\rho_g D_t\frac{\partial y_j}{\partial x_i}H_j\right)-\sum_{i=1}^{3}\frac{\partial}{\partial x_i}\left(\lambda_t\frac{\partial T}{\partial x_i}\right)=Q_{\text{rad}}, \quad (12)$$

with

$$H=\sum_{j=1}^{N}y_jH_j \qquad e_k=\frac{1}{2}\sum_{i=1}^{3}U_i^2. \quad (13)$$

The first term on the lefthand side of the energy equation expresses the convective transport of enthalpy, turbulent energy, and kinetic energy; the second term determines the diffusional enthalpy transport; the third term accounts for turbulent heat conduction. On the righthand side of the equation, we find the amount of radiative heat transfer per unit of volume.

The energy equation can be transformed into

$$\sum_{i=1}^{3}\rho_g U_i\left(\frac{\partial}{\partial x_i}(k+e_k)+C_p\frac{\partial T}{\partial x_i}\right)-\sum_{i=1}^{3}\rho_g D_t\sum_{j=1}^{N}C_{pj}\frac{\partial y_j}{\partial x_i}\frac{\partial T}{\partial x_i}=\sum_{i=1}^{3}\frac{\partial}{\partial x_i}\left(\lambda_t\frac{\partial T}{\partial x_i}\right)+\sum_k(-\Delta H_k r_{rk})+Q_{\text{rad}}, \quad (14)$$

in which the heat of combustion is found explicitly on the righthand side of the equation.

The Navier-Stokes equations are to be solved in an integration grid with small volumes compared to the total furnace volume. With the current computer capacities, use of the Hottel and Sarofim zone method for radiative heat transfer, with Monte-Carlo-based calculation of the view factors, is nearly impossible due to the large amount of CPU time needed. Therefore, the six-flux De Marco and Lockwood (1975) model is used for calculating the radiation intensity between the grid volumes. This model performs well for short-distance radiative heat transfer as encountered in the integration grid with small volumes (Detemmerman and Froment, 1998).

The total diffusivity, D_t, the total conductivity, λ_t and the total viscosity, μ_t, are calculated as the sum of the corresponding molecular and turbulent properties:

$$D_t=D_m+D_{\text{turb}} \quad (15)$$

$$\lambda_t=\lambda_m+\lambda_{\text{turb}} \quad (16)$$

$$\mu_t=\mu_m+\mu_{\text{turb}}. \quad (17)$$

The turbulent properties are calculated from the turbulence model or closure model. Use is made of the k-ϵ model (Jones and Launder, 1972), in which k represents the turbulent kinetic energy and ϵ represents the dissipation of k.

The k-ϵ model consists of two conservation equations:

$$\sum_{i=1}^{3}\frac{\partial}{\partial x_i}\left(\rho_g U_i k\right)=\sum_{i=1}^{3}\frac{\partial}{\partial x_i}\left(\mu_t\frac{\partial k}{\partial x_i}\right)+P_k-\rho_g\epsilon \quad (18)$$

$$\sum_{i=1}^{3}\frac{\partial}{\partial x_i}\left(\rho_g U_i\epsilon\right)=\sum_{i=1}^{3}\frac{\partial}{\partial x_i}\left(\frac{\mu_t}{1.33}\frac{\partial\epsilon}{\partial x_i}\right)+P_\epsilon-1.92\rho_g\frac{\epsilon^2}{k}, \quad (19)$$

with

$$P_k=\sum_{i=1}^{3}\sum_{j=1}^{3}\mu_t\left(\frac{\partial U_i}{\partial x_j}+\frac{\partial U_j}{\partial x_i}\right)\frac{\partial U_i}{\partial x_j} \quad (20)$$

$$P_\epsilon=1.44\frac{\epsilon}{k}P_k. \quad (21)$$

The turbulent viscosity μ_{turb} can be calculated from the turbulent energy and the dissipation of turbulent energy according to the Prandtl-Kolmogorov expression:

$$\mu_{\text{turb}}=0.09\rho_g\frac{k^2}{\epsilon}. \quad (22)$$

Next, the other turbulent properties are obtained through the analogies between transport of energy, mass, and momentum:

$$\frac{\lambda_{\text{turb}}}{\lambda_m}=\frac{D_{\text{turb}}}{D_m}=\frac{\mu_{\text{turb}}}{\mu_m}. \quad (23)$$

Combustion

The combustion of fuel gas in long-flame burners is considered to be a noninstantaneous reaction, resulting in concentration profiles for fuel-gas and flue-gas components in flame and furnace. These profiles are calculated from the Reynolds averaged continuity equations for the different components:

$$\sum_{i=1}^{3}\frac{\partial}{\partial x_i}\left(\rho_g U_i y_j\right)=\sum_{i=1}^{3}\frac{\partial}{\partial x_i}\left(\rho_g D_t\frac{\partial y_j}{\partial x_i}\right)+R_jM_j. \quad (24)$$

The first term on the righthand side of the equation represents the diffusion of the components. This term is included for the sake of generality. The integration grid for solving the equations is too coarse to adequately incorporate diffusion. Excessive computer memory and calculation time requirements prohibit adapting the grid size.

Calculation of the net production rate (second term on the righthand side of the equation) of the flue-gas components

Table 1. Furnace Dimensions and Operating Conditions

Furnace	
Height (m)	8
Length (m)	12
Width (m)	3
Thickness of refractory (m)	0.16
Thickness of insulation (m)	0.075
Number of burners	20
Reactor coils	
Number of reactors	4
Reactor type	4/2/1 split coil
Number of passes	2/1/3
External tube diameter (10^{-2} m)	8/12/16
Internal tube diameter (10^{-2} m)	7/10/15
Firing conditions	
Fuel gas (ton/h)	1.5
Oxygen excess (%)	1.5
Fuel-gas composition (wt. %)	
Hydrogen	5.5
Methane	85.3
Ethane	2.2
Propane	1.2
$CO+CO_2$	1.3
Total heat input, MW	22.5
Reactor operating conditions	
Feedstock	Naphtha
Feedstock composition (wt. %)	
Paraffins (8 components)	39.2
Iso-Paraffins (29 components)	36.9
Naphthenes (21 components)	18.5
Aromatics (5 components)	5.4
Feedstock feed rate, (kg/h), (4 coils)	11,800
Steam dilution (kg/kg)	0.5
Coil inlet temperature (K)	823
Coil outlet pressure (atm)	1.75
Material properties	
Emissivity of furnace wall	0.5
Emissivity of tube skin	0.9
Thermal conductivity of refractory (W/m·K)	$0.0193+118.0\times10^{-6}\ T$(K)
Thermal conductivity of insulation (W/m·K)	$0.0452+111.1\times10^{-6}\ T$(K)
Thermal conductivity of tube skin (W/m·K)	$-1.257+4.327\times10^{-2}\ T$(K)

(Table 1) requires combustion kinetics to be proposed for methane, ethane, propane, and hydrogen. Use is made of a five-step mechanism:

$$CH_4+\frac{3}{2}O_2 \xrightarrow{1} CO+2H_2O \tag{25}$$

$$C_2H_6+\frac{5}{2}O_2 \xrightarrow{2} 2CO+3H_2O \tag{26}$$

$$C_3H_8+\frac{7}{2}O_2 \xrightarrow{3} 3CO+4H_2O \tag{27}$$

$$CO+\frac{1}{2}O_2 \xrightarrow{4} CO_2 \tag{28}$$

$$H_2+\frac{1}{2}O_2 \xrightarrow{5} H_2O. \tag{29}$$

The Westbrook and Dryer (1981) kinetics were applied:

$$r_{r,1}=1.5\times10^{7.2}\exp\left(-\frac{125{,}604}{RT}\right)C_{CH_4}^{-0.3}C_{O_2}^{1.3} \tag{30}$$

$$r_{r,2}=1.3\times10^{12}\exp\left(-\frac{125{,}604}{RT}\right)C_{C_2H_6}^{0.1}C_{O_2}^{1.65} \tag{31}$$

$$r_{r,3}=10^{12}\exp\left(-\frac{125{,}604}{RT}\right)C_{C_3H_8}^{0.1}C_{O_2}^{1.65} \tag{32}$$

$$r_{r,4}=10^{14.6}\exp\left(-\frac{167{,}472}{RT}\right)C_{CO}C_{H_2O}^{0.5}C_{O_2}^{0.25}. \tag{33}$$

The hydrogen combustion is assumed to be instantaneous.

The eddy breakup model of Spalding (1972), which describes the turbulent mixing, is used. In this model, the reaction mixture of fuel gas and combustion air is assumed to consist of eddies containing the reaction components. The eddies break down to a level at which reaction is possible. Slow eddy breakup determines the rate of reaction and thus the consumption of fuel gas and the length of the flame. A mixing time scale is calculated from the k-ϵ model, based on an analogy between eddy breakup and the decay of turbulent energy (Hinze, 1959):

$$\tau_m^{-1}=4\frac{\epsilon}{k}. \tag{34}$$

Since mixing and reaction occur sequentially, mixing time and reaction time can be added, resulting in the following expression for the overall rate:

$$r_{t,k}=\left(\frac{1}{r_{r,k}}+\frac{M_{C_iH_j}}{r_{m,k}}\right) \tag{35}$$

for reactions 1 to 4, and

$$r_{t,5}=\frac{r_{m,5}}{M_{H_2}}. \tag{36}$$

The mixing rates r_m are calculated from

$$r_{m,k}=\frac{\rho_g}{\tau_m}\min\left(y_{C_iH_j},\frac{b}{a}y_{O_2}\right), \tag{37}$$

which shows that the breakup of the limiting reacting component is rate determining.

Calculation of the Flue-Gas Flow Pattern

Integration of the CFD model equations in the furnace is based on a finite-volume technique. A three-dimensional integration grid is constructed, starting from a representative cross section of the furnace. This cross section is filled with a number of nonstructured surface cells. Nonstructured grids are chosen in order to be able to accurately account for the presence of the reactor tubes and burner inlets in the furnace. By connecting consecutive two-dimensional grids, a three-dimensional grid of irregular prisms is constructed.

The basic Navier-Stokes equations and turbulence model equations can be written in matrix formulation:

$$\frac{\partial F}{\partial x}+\frac{\partial G}{\partial y}+\frac{\partial H}{\partial z}=\frac{\partial F'}{\partial x}+\frac{\partial G'}{\partial y}+\frac{\partial H'}{\partial z}+P. \quad (38)$$

The lefthand side of the matrix formulation contains the convective terms of the basic equations; the righthand side contains the viscous terms and a production or source term P.

The first step in discretizing the basic equations is to integrate the matrix formulation over a volume cell of the three-dimensional grid:

$$\int_{V_i}\left(\frac{\partial F}{\partial x}+\frac{\partial G}{\partial y}+\frac{\partial H}{\partial z}\right)dV=\int_{V_i}\left(\frac{\partial F'}{\partial x}+\frac{\partial G'}{\partial y}+\frac{\partial H'}{\partial z}\right)dV + \int_{V_i} P dV. \quad (39)$$

The convective terms of the equations are treated using a first-order flux difference-splitting method (Lombard et al., 1982). For the viscous parts of the equations a central difference scheme is used. The source terms contain three types of contributions: the diffusional enthalpy transport is neglected; the contribution of radiative heat transfer is calculated according to the De Marco-Lockwood six-flux model (De Marco and Lockwood, 1975); the contribution of reaction heat is treated following the flux difference-splitting concept. Detailed information is found in De Saegher et al. (1996) and Detemmerman and Froment (1998).

The resulting set of equations is solved using a Gauss elimination method. Convergence is reached when the residual sum of squares calculated from the normalized differences between the right- and lefthand sides of the preceding equation has dropped under a given value.

Calculation of the Concentration Profiles in the Furnace

The concentration profiles of methane, ethane, propane, oxygen, and carbon monoxide determine the rate of combustion and thus the combustion heat release in the different volume elements in the integration grid. They are calculated by solving the continuity equations for all species j in each integration volume V_i in the furnace. Again, a first order splitting concept followed by a Gauss elimination method is used to solve the equation.

Boundary Conditions

All variables, except the pressure, are prescribed at the inlet of the furnace. The pressure is prescribed at the outlet of the furnace.

Impermeability for the mass flows is imposed at the walls. The flow is considered to be parallel to the wall. In the vicinity of the wall, the k-ϵ model equations are no longer valid. They are replaced by so-called wall functions to determine values for k and ϵ:

$$k=\frac{U_\tau^2}{\sqrt{C_\mu}} \quad (40)$$

$$\epsilon=\frac{U_\tau^3}{\kappa y_1}, \quad (41)$$

where U_τ represents the friction velocity:

$$U_\tau=\sqrt{\frac{\tau_\omega}{\rho_g}}, \quad (42)$$

determined by the wall shear stress:

$$\tau_\omega=\mu_{\text{turb}}\frac{\partial U}{\partial y}, \quad (43)$$

in which the turbulent viscosity is calculated from:

$$\mu_{\text{turb}}=C_\mu\frac{k^2}{\epsilon}\rho_g. \quad (44)$$

The distance to the wall is given by y_1.

Overview of the Calculations

A global flow chart of the calculations is given in Figure 1, and an extended outline of the calculation is given by Detemmerman and Froment (1998).

Two integration grids are constructed in the furnace. The first integration grid consists of rather large surface and volume zones. This grid is used for the coupled simulation of furnace and reactor. The view factors between these zones are calculated and initial temperature and heat-flux estimates are made. The second integration grid, the nonstructured grid, is used to calculate the flue-gas flow pattern and flue-gas concentration profiles. Based on initial temperature estimates for furnace wall and reactor tube skin, the concentration profiles in the flue gas and the net radiative heat exchanges are calculated. This allows us to make an initial calculation of the flue-gas flow pattern. A coupled simulation of furnace and reactor tubes is performed with this flow pattern, resulting in improved zone temperature and heat-flux profiles. Next, the concentration profiles and flow patterns in the furnace can be updated. This cycle is repeated until convergence is reached. When the residual sum of squares calculated from the normalized differences between the right- and lefthand sides of the Navier-Stokes equations, the turbulence model equations and the continuity equations for the flue-gas components have dropped below a given value, the calculations are stopped. Calculations were performed on an IBM/RS6000 workstation, requiring several hundred hours of CPU-time.

Furnace Geometry and Operating Conditions

The main dimensions and the operating conditions of the naphtha-cracking furnace are summarized in Table 1, as are the reactor coil dimensions. Four reactor coils of the 4/2/1

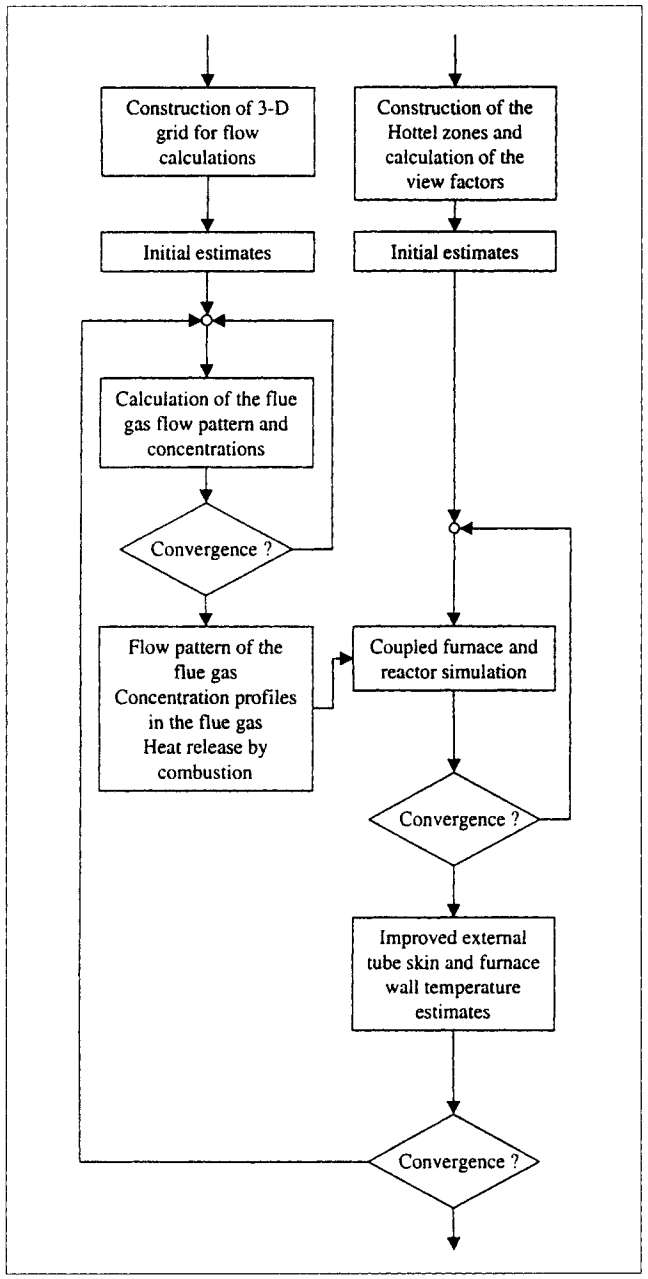

Figure 1. Calculations (Detemmerman and Froment, 1998).

split type (4 inlets and 1 outlet for each reactor coil) are suspended in the center of the furnace. The process gas makes six passes through the furnace. A front view and a top view of half a furnace are shown in Figure 2. The different tubes of the reactor coil have different diameters due to the split-coil concept. The composition of the naphtha cracked in these coils is also summarized in Table 1. For the reactor-coil calculations, a feed of 8 different paraffins, 29 iso-paraffins, 21 naphthenes, and 5 aromatics is taken into account.

The furnace is heated by means of 20 long-flame burners in the furnace floor. The position of these burners is indicated in Figure 2. The fuel-gas composition is given in Table

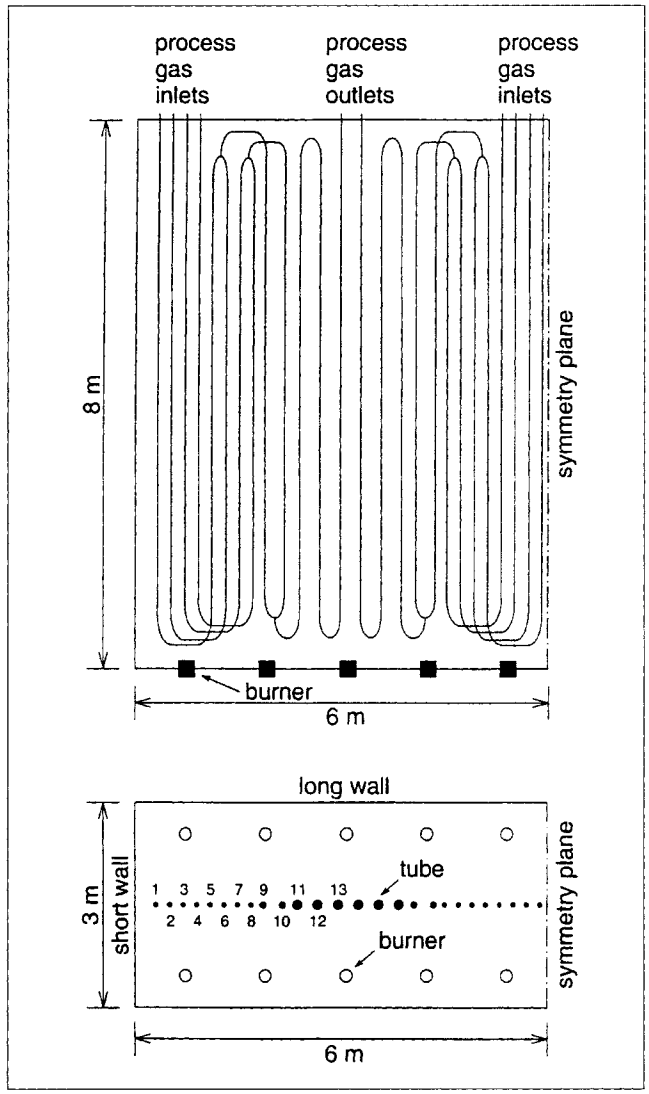

Figure 2. Naphtha cracking furnace: front and top views.

1. The flue gas leaves the furnace through an opening that extends the entire length of the long furnace wall (Figure 3).

For the coupled simulation of the coupled furnace and reactor coils, the furnace is divided into 27 isothermal zones by means of 8 planes parallel to the furnace bottom and 2 planes parallel to the long furnace walls, as shown in Figure 3. For reasons of symmetry, only half the furnace has to be calculated, resulting in a total number of 312 zones: 234 tube skin zones, 51 furnace wall zones, and 27 gas volume zones. For the calculation of the flue-gas flow pattern, the bottom of the furnace is divided into 927 surface elements, as shown in Figure 3. Reactor tubes and burner openings can easily be located in the constructed grid. The furnace is divided by means of 51 planes parallel to the furnace bottom, resulting in an integration grid with a total of 48,204 finite integration volumes.

Results and Discussion

The simulation results are given in Table 2 and shown in Figures 4 to 13.

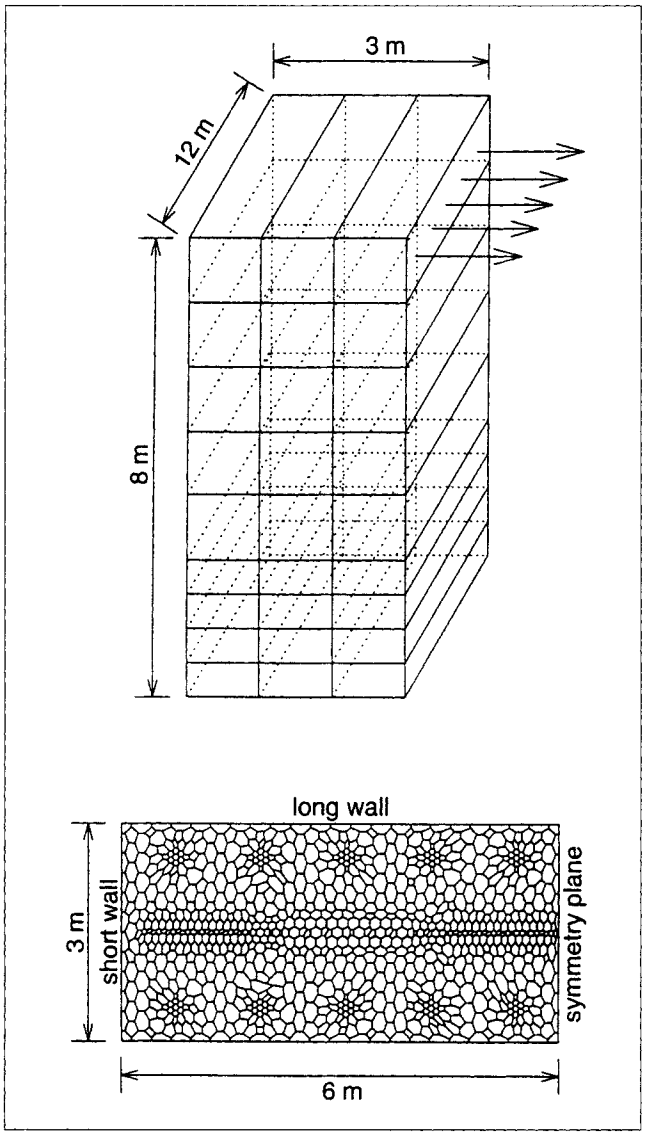

Figure 3. Hottel zones and flow calculation grid (horizontal cross section).

Table 2. Simulation Results

Coupled furnace reactor simulation	
Flue gas outlet temperature (K)	1,400
Furnace efficiency (%)	44
Maximum heat flux (kW/m^2)	133
Average heat flux (kW/m^2)	74
Coil outlet temperature (K)	1,100
Maximum tube-skin temperature (K)	1,333
Coil pressure drop (atm)	0.45
Naphtha conversion (%)	90.3
Ethylene yield (wt. %)	26.2
Propylene yield (wt. %)	16.5
Cracking severities	
C_2H_4/CH_4	1.95
C_3H_6/CH_4	1.23
C_3H_6/C_2H_4	0.63
C_{3^-}/C_3H_6	3.70
Coil residence time (s)	0.45
Maximum coking rate (kg/m^2·s)	1.18×10^{-6}
Flow pattern calculation	
Maximum flue-gas velocity (m/s)	16
Flue-gas outlet velocity (m/s)	7
Maximum flame temperature (K)	2,100

considered simultaneously. Figure 5 shows flue-gas velocity vectors projected on a vertical cross section of the furnace, while Figure 6 shows flue-gas velocity vectors projected on a horizontal cross section of the furnace. The vertical plane in Figure 5 is situated 0.78 m from the short furnace wall, as is indicated in Figure 6. At this position there are two burner openings in the furnace floor, one at each side of the reactor tube row. The horizontal plane in Figure 6 is situated at a furnace height of 1.25 m, as indicated in Figure 5. It will be seen later that this location corresponds to the position at which the highest flame temperatures are obtained.

In Figure 5, the burner positions are easily located by the high velocity of the fuel gas and the combustion air entering the furnace through the small burner openings. Velocities on the order of 10 m/s are calculated just above the burner openings. It is also seen in Figure 5 that the highest flue gas velocities in the flame are calculated about 1 m above the furnace floor. Acceleration of the flue gas is due to the flue-gas expansion caused by both the burning of the fuel gas (re-

Flue-gas velocity field

Figure 4 shows the calculated three-dimensional flue-gas velocity vectors in a horizontal cross section of the furnace at a height of 1.33 m. Right above the burner inlet openings, the velocity vectors have only a vertical component as a consequence of the high vertical velocity of the fuel gas entering the furnace through the small burner openings. Surrounding these vertical velocity vectors is a region with velocity vectors, each with a smaller vertical and a limited horizontal component. The flue-gas velocity vectors near the furnace walls and in the center of the furnace are very small. Although recirculation of the flue gas might be expected because of the high inlet velocities, no such phenomena are calculated in the constructed grid.

In order to have an even clearer view of the flow field a two-dimensional presentation of the three-dimensional results is necessary. To this end, Figures 5 and 6 have to be

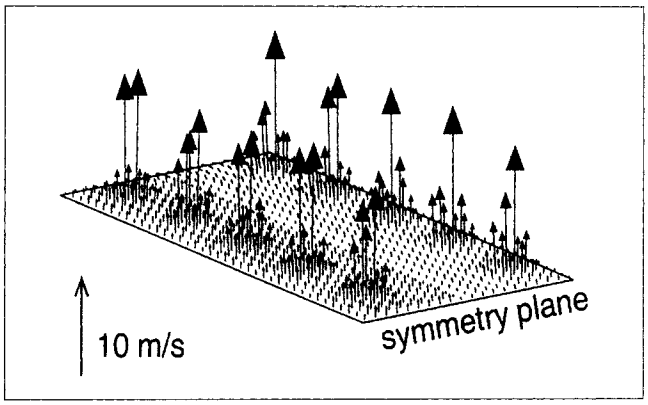

Figure 4. 3-D flue-gas velocity vectors in a horizontal cross section of the furnace at a height of 1.33 m.

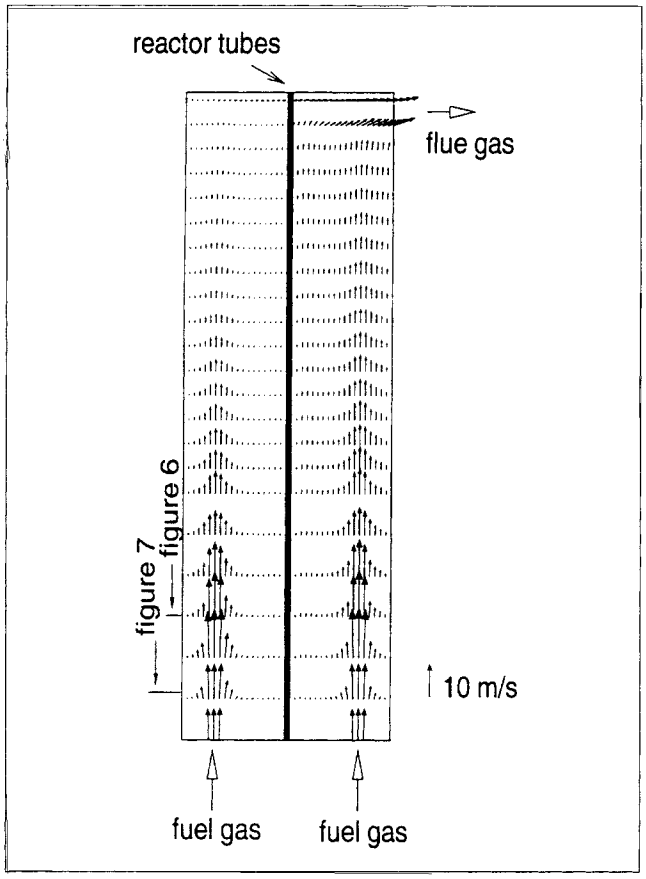

Figure 5. Flue-gas velocity vectors projected on a vertical furnace cross section, parallel to the short wall of the furnace at a distance of 0.78 m.

The cross section is viewed from the short-wall side of the furnace.

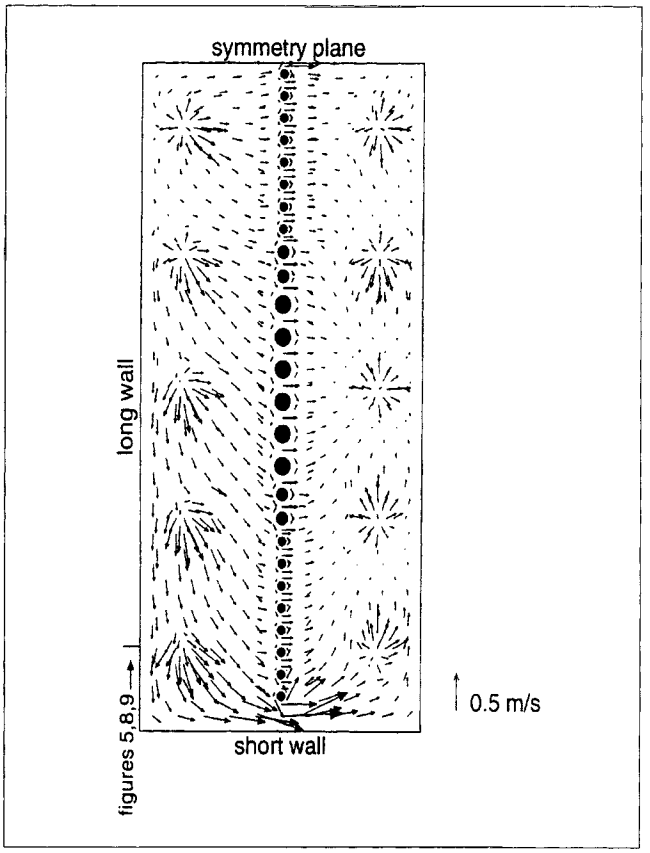

Figure 6. Flue-gas velocity vectors projected on a horizontal furnace cross section at a height of 1.52 m.

The cross section is viewed from the top of the furnace.

action stoichiometry), but mainly by the rise of the temperature. It will be seen later that between the furnace floor, where the cold fuel-gas and combustion air enter, and the hot flame center, a flue-gas temperature increase of nearly 2000 K is calculated. Maximum velocities on the order of 15 m/s are calculated at a height of about 1 m. The influence of the flames is felt over the entire furnace height because flue-gas velocities above the burner openings remain at a higher level than the flue-gas velocities in the center of the furnace.

The flue gas leaves the furnace through an opening in the long sidewall at the righthand side of the furnace, as seen in Figure 5. As a consequence, the flue-gas flow pattern in the furnace is not identical on both sides of the reactor tubes. Over the furnace height, flue gas flows from the lefthand side to the righthand side of the furnace. This can be concluded from Figure 5, as the flue-gas velocities on the lefthand side of the reactor-tube row steadily fall with furnace height, while the flue-gas velocities on the righthand side of the reactor-tube row steadily rise with furnace height. At a furnace height of 4 m, two-thirds of the total amount of flue-gas already flows through the righthand side of the furnace where the flue-gas outlet opening is situated. At the top of the furnace, near the flue gas outlet, this flue-gas distribution has changed to 85% on the righthand side and 15% on the lefthand side. This change has a considerable influence on the flue-gas velocities on both sides of the furnace. When the average flue-gas velocity over a line parallel to the short furnace wall and at the position of two facing burners is calculated, a value of 3.21 m/s is obtained on the lefthand side of the furnace, while a value of 3.44 m/s is obtained on the righthand side, for a furnace height of 1.5 m. Halfway through the furnace, at a height of 4 m, these values have changed to 1.36 m/s and 2.22 m/s, respectively. At a height of 7.5 m, where the flue-gas outlet is situated, average values of 0.41 m/s and 1.88 m/s, respectively, are calculated. It must be remarked that these line-averaged flue-gas velocities are considerably higher than the values obtained when the flue-gas velocities are averaged over a horizontal plane in the furnace. For example, at a furnace height of 4 m, surface-averaged values of 0.58 m/s and 1.30 m/s are calculated on the lefthand and the righthand sides of the furnace, respectively. At the flue-gas outlet, these values have changed to 0.26 m/s and 1.49 m/s, respectively.

This uneven distribution of flue gas in the furnace can have an influence on the circumferential tube-skin temperature profiles, which might be nonsymmetrical (Heynderickx et al., 1992). This, in turn, will influence the circumferential coke formation and the run length of the furnace (Heynderickx and Froment, 1996).

Figure 6, which shows the flue-gas velocity vectors projected on a horizontal cross section at a furnace height of

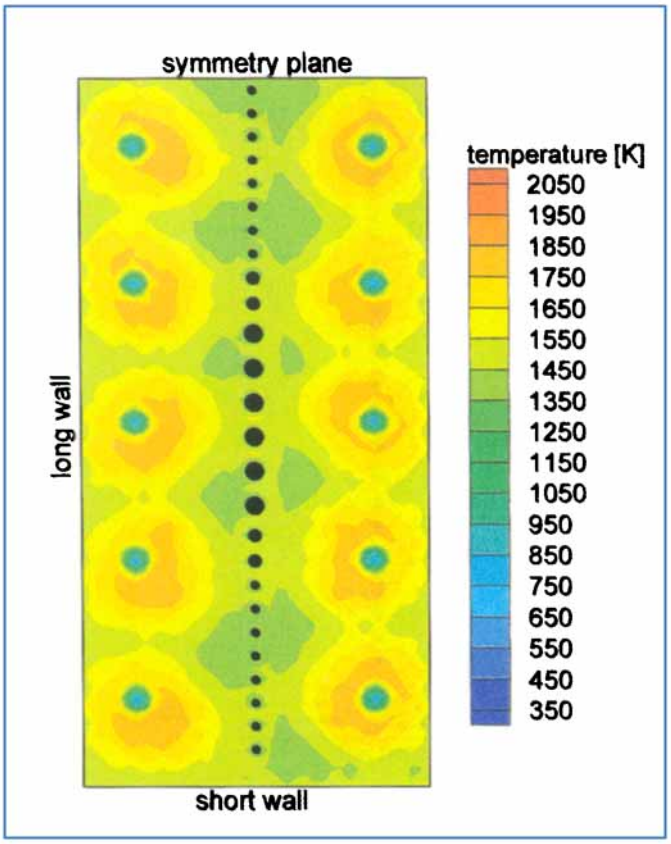

Figure 7. Flue-gas temperature field in a horizontal furnace cross section at a height of 0.61 m.

The cross section is viewed from the top of the furnace.

1.25 m, shows how this flue-gas flow from the lefthand side to the righthand side takes place. Although it is seen that some of the flue gas flows in between the tubes, the flue gas has a clear tendency to move "around" the reactor tubes, and pass from one furnace half to the other by flowing in between the short furnace wall and the first reactor tube. This can be explained by the fact than the distance between the wall and first reactor tube (285 mm) is considerably higher than the distance between two tubes (124 mm). The same flue-gas flow patterns are calculated higher up in the furnace.

This specific flow pattern has an influence on the flames near the short furnace wall, on both the left- and righthand sides. Due to the high horizontal velocity component (up to 1 m/s) of the flue gas flowing in between the short furnace wall and the outer reactor tube from the left- to the righthand side of the furnace, the flames on the lefthand side have a tendency to "bend" toward the short furnace wall, while the flames on the righthand side have a tendency to "bend" away from the short furnace wall. This means that they are asymmetrical compared to the center line through the burner opening parallel to the short wall of the furnace. This is illustrated in Figure 7, which presents the temperature field in a horizontal cross section of the furnace taken at a furnace height of 0.61 m. At the lefthand side of the furnace, the flame zone with the highest flame temperatures has a larger surface at the flame side facing the short furnace wall than at the flame side facing the interior of the furnace; the opposite effect is found at the righthand side. This "bending" effect has not yet fully disappeared for the burners positioned near the furnace center line. Finally, it must be remarked that the horizontal components of the flue-gas velocity vectors at any position in the flames are not higher than 0.5 m/s, compared to vertical flue-gas velocity vector components, which rise to 15 m/s.

Flue-gas temperature field and concentration profiles

Figure 7 shows how the temperature in the furnace drops, moving from the flames toward the tube row. Another interesting aspect is the temperature differences of the flue gas along the tube row. In between two facing burners, one on each side of the furnace, a zone of high flue-gas temperatures is calculated around the tube row. In between a group of four burners, two on each side of the furnace, a zone of lower flue-gas temperatures is calculated around the tube row. This effect shows that the amount of radiative heat transfer is indeed, among other things, determined by the distance between the source (flame) and the receptor (tube).

Figures 8a and 8b are studied at the same time. Figure 8a shows the percentage of residual methane in a vertical cross section of the furnace, taken at the same position as the vertical cross section in Figure 5. Methane is chosen for representation, as it is the principal fuel-gas component. Figure 8b shows the corresponding temperature profiles. Only half the furnace height is shown. The mass fraction of methane in the fuel-gas and combustion-air mixture that is fed to the burners is no more than about 4 wt. %. The residual methane curve of 4 wt. % in Figure 8a therefore corresponds to unburned fuel gas. In the zone enclosed by this curve, the fuel-gas/combustion-air mixture is heated from 300 K to about 500 K, as seen in Figure 8b. This zone is about 0.7 m high and 0.2 m wide. The heating of the mixture in this zone is due to radiation and heat conduction in the flame. Ignition occurs next, and flame temperatures rise very quickly due to the release of combustion heat. Temperatures up to 1,750 K are calculated around the 4 wt. % residual methane curve. The residual methane curves of 2 wt. % and 0.1 wt. % correspond to 50% and 97.5% of the total amount of methane burnt in the flame. In between these two curves, the highest flame temperatures are obtained above the burner outlet opening. This zone with high flame temperatures is a long (1 m), small (0.3 m) zone, indicating that the vertical component of the flue-gas velocity vectors is much larger than the horizontal one, as was already found when studying Figures 5 and 6. A maximum flame temperature of 2,050 K is calculated. Figure 8b shows that at a furnace height of 3 m there are still considerable temperature differences (200 to 300 K) when moving from the furnace wall toward the reactor tubes. At a furnace height of 4 m these differences are almost completely flattened out. Furthermore, it is also clear that the flame is "confined" by the furnace wall at one side, while it can freely expand at the side facing the reactor-tube row, resulting in asymmetrical flames compared to the center line through the burner opening parallel to the long furnace wall. This can also be observed in Figure 7, which shows the temperature field in a horizontal cross section of the furnace.

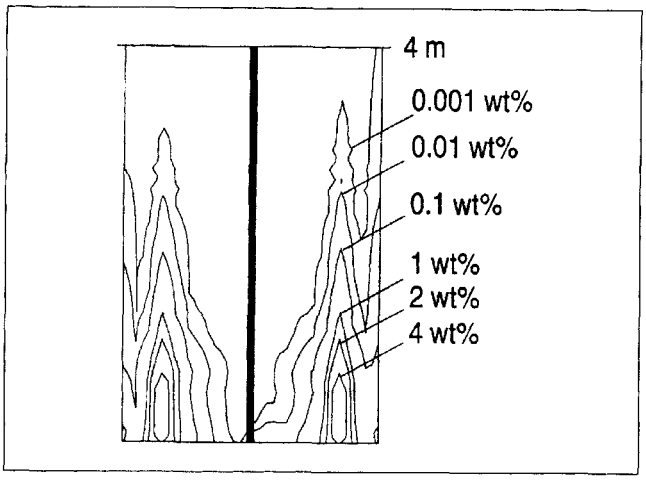

(a)

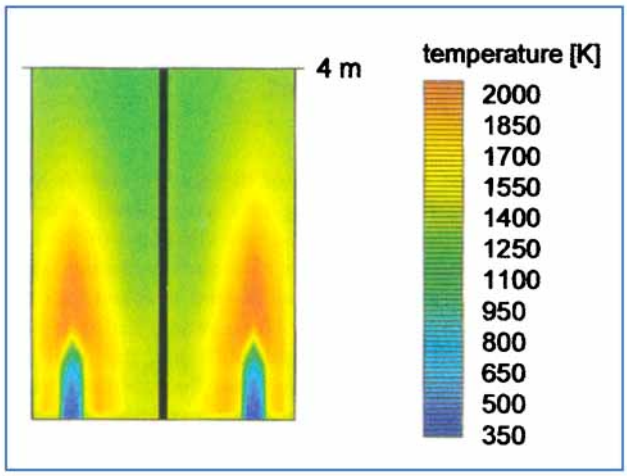

(b)

Figure 8. (a) Methane concentration profiles in a vertical cross section, parallel to the short wall of the furnace at a distance of 0.78 m; (b) temperature field in a vertical cross-section, parallel to the short wall of the furnace at a distance of 0.78 m.

All the discussed phenomena are summarized in Figure 9, which presents a complete three-dimensional view of the temperature field in the furnace.

Reactor-tube profiles

Figure 10 shows the heat-flux profile from the furnace to the external reactor-tube skin, for the coil closest to the short furnace wall, with tube passes numbered 1 to 13, as shown in Figure 2. It is clearly seen that the reactor coil makes six passes through the furnace. Three heat-flux maxima on the order of 130 kW/m^2_{ext}, are calculated when the reactor coil passes the bottom of the furnace where radiative heat transfer from the hot flue gas and the hot furnace walls is high. At the top of the furnace, where temperatures and therefore radiative transfers are lower, the flux profiles go through minima on the order of 50 kW/m^2_{ext}. With the 4/2/1 split-coil concept, the process gas is split up into four reactor tubes for both the first (tubes 1 to 4) and second passes (tubes 5 to 8) of the process gas through the furnace. Heat-flux differences of up to 10 kW/m^2_{ext} (10%) between the four inlet reactor tubes are calculated for one coil. These differences are due

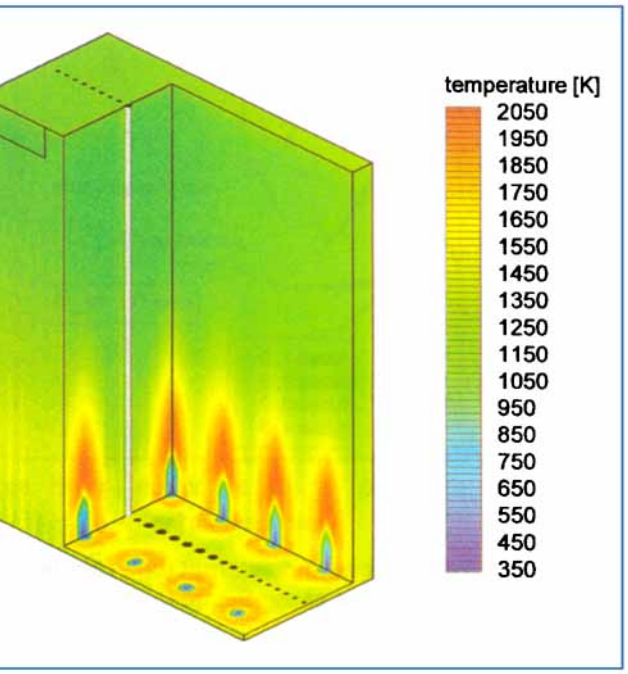

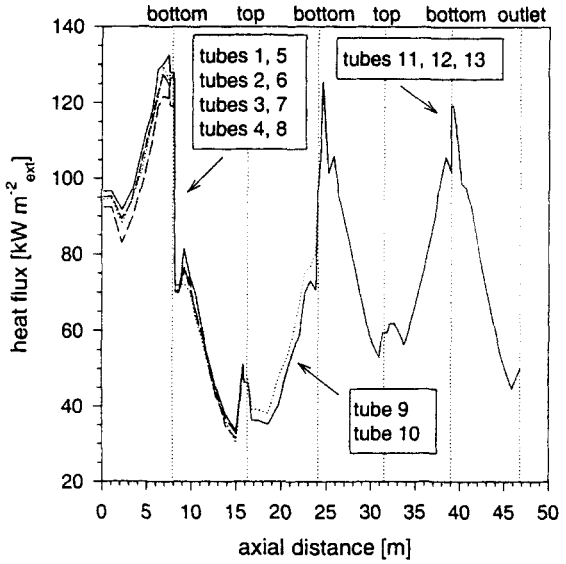

Figure 10. Heat-flux profiles along the coil.

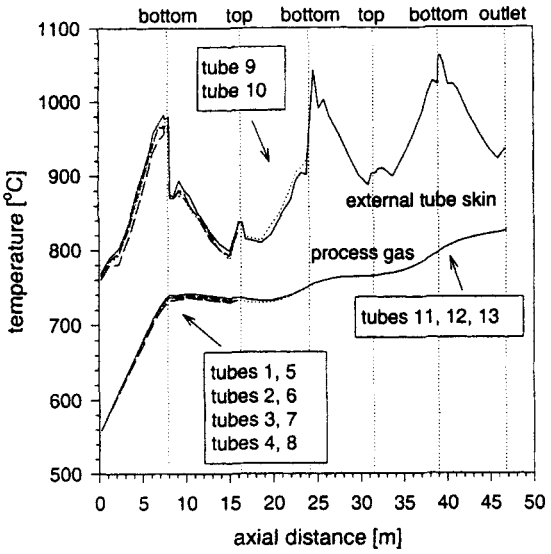

Figure 11. Process gas and external tube skin temperature profiles along the coil.

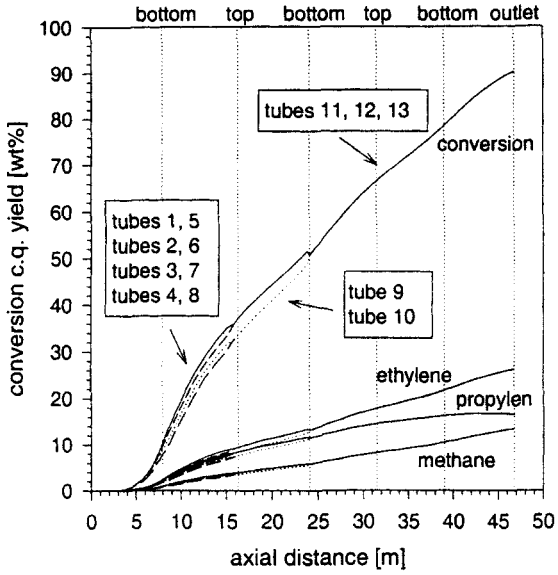

Figure 12. Naphtha conversion and ethylene/propylene yields along the coil.

to the different geometrical positions of these four tubes in the furnace with respect to the furnace walls and to the burner positions. The distance between the short furnace wall and the reactor tubes increases from tube 1 to tube 4. This results in smaller radiative heat transfer, as radiative heat transfer is also determined by the distance between the emitter and receptor.

Nevertheless, fluxes to tube 3 are higher than fluxes to tube 2 in the bottom of the furnace. This is due to the position of the first burner, located closest to reactor tube 3. This effect was discussed already in Figure 7. The heat-flux values for the coil positioned in the center of the furnace (which are not shown here) differ slightly from the heat-flux values for the outer coil. Again, this difference is caused by the position of reactor tubes compared to furnace wall and burners. However, the global form of the heat-flux profiles remains unchanged. The differences in heat fluxes to the parallel reactor tubes result in differences in tube-skin temperature profiles and process-gas temperature profiles, as shown in Figure 11. The form of the tube-skin temperature profile follows that of the heat-flux profile, with maxima in the furnace bottom and valleys in the furnace top. However, although the highest heat fluxes are calculated at the beginning of the reactor coil, the highest tube-skin temperatures are calculated at the end of the coil. This is off course due to the rising process gas temperatures changing from 823 K to 1,100 K in the reactor coil. A maximum tube-skin temperature of 1,330 K is calculated in the last bottom bend of the coil.

Figure 12 shows the corresponding conversion profile of the naphtha feed and the yield profiles for ethylene, propylene, and methane throughout the reactor tube. Naphtha conversions up to 90% are achieved, with corresponding ethylene yields of 26 wt. % and propylene yields of 15.5 wt. %. Cracking severities are given in Table 2.

Finally, Figure 13 shows the calculated coke formation rates in the reactor tubes. The highest values are obtained at the coil positions where the tube skin temperatures are highest, that is, in the last bottom bend of the reactor coil. A maximum coking rate of 1.8×10^{-6} kg/m^{2}s is calculated. The coking-rate values allow calculation of the thickness of the coke layer that is formed on the inner tube surface during operation. This coke layer forms an additional resistance to heat transfer from furnace to reactor. As a result, if the naphtha conversion is to be kept at a constant value, the total heat input in the furnace, and thus the total flue-gas flow, has to rise with time. Furthermore, the growing coke layer reduces the tube cross section. When the process-gas feed rate is kept constant, the pressure drop over the coil will rise. As the reactor coil outlet pressure is imposed, the coil inlet pressure has to rise during operation.

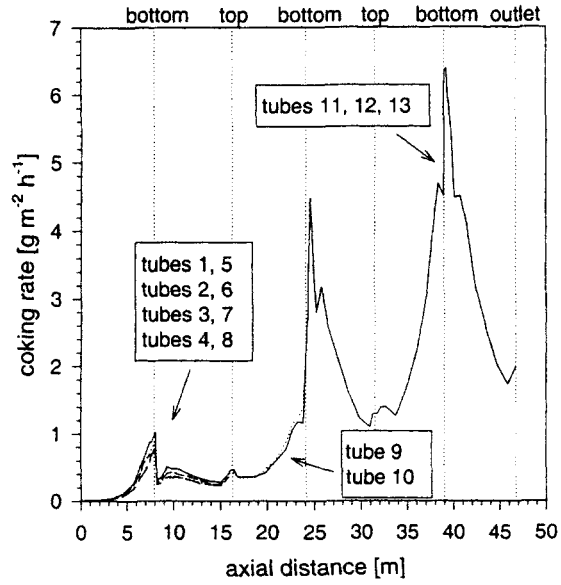

Figure 13. Coking-rate profiles along the coil.

A so-called run-length simulation of the furnace (Plehiers et al., 1990) can also be performed with the software used to obtain the simulation results presented earlier. In a run-length simulation, the presence of the gradually growing coke layer in the tubes is taken into account. The heat input in the furnace and the process-gas inlet pressure are gradually increased. Convergence of the calculation cycle presented in Figure 1 has to be reached for each time step, taking into account the changing operating conditions. The calculations are stopped when the tube-skin temperature or the process-gas inlet pressure reaches too high a value.

Conclusions

Simulation packages for the coupled simulation of cracking furnaces and cracking reactors were combined with a simulation package for the calculation of three-dimensional flue-gas flow patterns in cracking furnaces, to simulate a naphtha cracking furnace with 4/2/1 split-coil reactors and fired with long-flame burners. Typical flue-gas circulation profiles in the furnace are calculated. However, no large vertical recirculation profiles of the flue gas in the furnace are obtained. An extremely uneven distribution of the flue gas over the two furnace halves is obtained because of the asymmetric position of the flue-gas outlet. Furthermore, the flow profiles reveal a flue-gas "shortcut" flow between the outer reactor tubes of the reactor tube row and the short furnace walls. Another point of interest is the influence of the uneven flue-gas distribution over the furnace halves on the circumferential tube-skin temperatures.

Acknowledgments

Geraldine Heynderickx and Guy Marin are grateful to the "Fonds voor Wetenschappelijk Onderzoek-Vlaanderen" (FWO-N) for financial support of the CFD Research. Arno Oprins is grateful to DSM for a research assistantship.

Notation

a = stoichiometric reaction coefficient
A_i = surface area of zone i, m^2
b = stoichiometric reaction coefficient
C_c = coke concentration, mol/m^3
C_iH_j = hydrocarbon component
C_p = specific heat of total gas flow, J/kg·K
C_μ = wall function constant
c_{pj} = specific heat of component j, J/mol·K
D_m = molecular diffusivity, m^2/s
D_{turb} = turbulent diffusivity, m^2/s
D_t = total diffusivity ($D_m + D_{\text{turb}}$), m^2/s
d_t = reactor tube diameter, m
E_i = black-body emissive power of zone i, W/m^2
e_k = specific kinetic energy, J/kg
F_j = molar flow rate of species j, mol/s
fr = friction factor, 1/m
G = total mass flux of process gas, kg/m^2·s
H = enthalpy, J/kg
H_j = enthalpy of formation for component j, J/kg
$-\Delta H_k$ = heat of reaction for reaction k, J/mol
k = turbulent kinetic energy, J/kg
M_j = molecular weight of component j, kg/mol
M_m = average molecular weight of hydrocarbon mixture, kg/mol
n_{kj} = stoichiometric coefficient for component j in reaction k
P_k = production of turbulent energy, W/m^3
P_ϵ = dissipation of turbulent energy equation source term, J/m^3·s^2
p_t = total pressure, Pa
Q = heat flux, W/m^2
Q_i = heat flux for zone i, W/m^2
Q_{rad} = net radiative heat exchange, W/m^3
R = universal gas constant, J/mol K
R_b = reactor-tube bend radius, m
R_c = rate of coke formation, mol/m^3
R_j = rate of formation of component j, mol/m^3·s
Re = Reynolds number
r_{mk} = mixing rate of reaction k, kg/m^3 s
r_{tk} = total rate of reaction k, kg/m^3 s
r_{rk} = reaction rate of reaction k, mol/m^3 s
T = temperature, K
T_i = temperature of zone i, K
U_i = velocity component in i-direction, m/s
U_τ = friction velocity, m/s
x_i = coordinate in i-direction, m
y_j = weight fraction of component j
y = distance to the wall, m
Z_iZ_j = total exchange area between zones i and j, m^2
z = axial reactor tube coordinate, m

Greek letters

α = unit conversion factor
σ = Stefan-Boltzmann constant, 5.7×10^{-8} W/m^2·K^4
ρ_g = gas density, kg/m^3
λ_m = molecular conductivity, W/m·K
λ_{turb} = turbulent conductivity, W/m·K
λ_t = total conductivity, ($\lambda_m + \lambda_{\text{turb}}$), W/m·K
μ_m = molecular viscosity, Pa·s
μ_{turb} = turbulent viscosity, Pa·s
μ_t = total viscosity ($\mu_m + \mu_{\text{turb}}$), Pa·s
ϵ = dissipation of turbulent kinetic energy, m^2/s^3
κ = wall function constant
τ_m = mixing time scale, s
τ_ω = wall shear stress, kg/m·s^2
Λ = angle, °

Literature Cited

De Marco, A. G., and F. C. Lockwood, "A New Flux Model for the Calculation of Radiation in Furnaces," *Riv. Combust.*, **29**, 184 (1975).

Dente, M., and E. Ranzi, *Pyrolysis: Theory and Industrial Practice*, Academic Press, San Diego (1983).

De Saegher, J. J., T. Detemmerman, and G. F. Froment, "Three-Dimensional Simulation of High-Severity Internally Finned Cracking Coils for Olefins Production," *Rev. Inst. Fr. Pet.*, **51**, 245 (1996).

Detemmerman, T., and G. F. Froment, "Three-Dimensional Coupled Simulation of Furnaces and Reactor Tubes for the Thermal Cracking of Hydrocarbons," *Rev. Inst. Fr. Pet.*, **53**, 181 (1998).

Heynderickx, G. J., G. G. Cornelis, and G. F. Froment, "Circumferential Tube Skin Temperature Profiles in Thermal Cracking Coils," *AIChE J.*, **38**, 1905 (1992).

Heynderickx, G. J., and G. F. Froment, "A Pyrolysis Furnace with Reactor Tubes of Elliptical Cross Section," *Ind. Eng. Chem. Res.*, **35**, 2183 (1996).

Hinze, J. O., *Turbulence: An Introduction to Its Mechanisms and Theory*, McGraw-Hill, New York (1959).

Hottel, H. C., and A. F. Sarofim, *Radiative Heat Transfer*, McGraw-Hill, New York (1967).

Jones, W. P., and B. E. Launder, "The Prediction of Laminarization with a Two-Equation Model of Turbulence," *AIAA J.*, **15**, 301 (1972).

Knudsen, J. G., and D. L. Katz, "Fluid Dynamics and Heat Transfer," McGraw-Hill, New York (1958).

Lombard, C. K., J. Oliger, and J. Y. Yang, "A Natural Conservative Flux Difference Splitting for the Hyperbolic Systems of Gas Dynamics," AIAA Paper 82-0976 (1982).

Nekrasov, B. B., *Hydraulics*, Peace Publishers, Moscow (1969).

Plehiers, P. M., and G. F. Froment, "Firebox Simulation of Olefin Units," *Chem. Eng. Commun.*, **80**, 81 (1989).

Plehiers, P. M., G. C. Reyniers, and G. F. Froment, "Simulation of the Run Length of an Ethane Cracking Furnace," *Ind. Eng. Chem. Res.*, **29**, 636 (1990).
Ranzi, E., M. Dente, S. Pierucci, and G. Biardi, "Initial Product Distribution from Pyrolysis of Normal and Branched Paraffins," *Ind. Eng. Chem. Fundam.*, **22**, 132 (1983).
Rao, M. V. R., P. M. Plehiers, and G. F. Froment, "Simulation of the Run Length of an Ethane Cracking Furnace," *Ind. Eng. Chem. Sci.*, **43**, 1223 (1988).
Reyniers, G. C., G. F. Froment, F.-D. Kopinke, and G. Zimmerman, "Coke Formation in the Thermal Cracking of Hydrocarbons, 4. Modeling of Coke Formation in Naphtha Cracking," *Ind. Eng. Chem. Res.*, **33**, 2584 (1994).
Spalding, D. B., "Mixing and Chemical Reaction in Steady Confined Turbulent Flames," Imperial College of Science and Technology, London, p. 649 (1972).
Sundaram, K. M., and J. V. Albano, "Design Pyrolysis Heaters using CFD Models," *Hydrocarbon Process.*, **7**, 79 (1997).
Westbrook, C. K., and F. L. Dryer, "Simplified Reaction Mechanisms for the Oxidation of Hydrocarbon Fuel in Flames," *Combust. Sci. Technol.*, **27**, 31 (1981).
Willems, P., and G. F. Froment, "Kinetic Modeling of the Thermal Cracking of Hydrocarbons, Part 1: Calculation of Frequency Factors," *Ind. Eng. Chem. Res.*, **27**, 1959 (1988a).
Willems, P., and G. F. Froment, "Kinetic Modeling of the Thermal Cracking of Hydrocarbons, Part 2: Calculation of Activation Energy," *Ind. Eng. Chem. Res.*, **27**, 1966 (1988b).

Manuscript received Mar. 8, 2000, and revision received July 10, 2000.